



Solvent-Free Synthesis of Zeolite Crystals Encapsulating Gold–Palladium Nanoparticles for the Selective Oxidation of Bioethanol

Jian Zhang, Liang Wang,* Longfeng Zhu, Qinming Wu, Chunyu Chen, Xiong Wang, Yanyan Ji, Xiangju Meng, and Feng-Shou Xiao*^[a]

The conversion of bioethanol into valuable products is an important area in the conversion of biomass. We demonstrate the successful synthesis of bimetallic gold–palladium (Au–Pd) nanoparticles encapsulated within S-1 zeolite crystals (AuPd@S-1) by a solvent-free strategy. This strategy allows highly efficient use of the noble metals, with more than 96% of the gold and palladium being loaded into the final samples. Electron microscopy characterization and investigations with probe molecules confirm that the Au–Pd nanoparticles are encapsulated inside the S-1 crystals. The AuPd@S-1 catalyst is very active for the aerobic oxidation of bioethanol, giving 100% conversion and 99% selectivity to acetic acid. Even in the presence of 90% water, the catalyst still gives a conversion higher than 80% and a selectivity of 95%. More importantly, the AuPd@S-1 catalyst exhibits excellent stability in the oxidation of bioethanol. These features are important for future practical applications of the AuPd@S-1 catalyst.

Because biomass is regarded as a renewable source of energy to reduce the need for fossil sources of oil, the conversion of biomass-derived feedstocks into valuable products is of great importance.^[1,2] One typical example is bioethanol, which has already been used as a fuel additive and has great potential for producing valuable products such as acetic acid.^[3–17] Conventionally, acetic acid is synthesized by carbonylation of methanol. This process is not considered green because it involves the use of CO and iodocompounds as catalytic mediators.^[8] Enzymatic oxidation of bioethanol could produce acetic acid, but enzymatic catalysts are not popular in chemical industry. Considering the very high output of bioethanol (more than 100 billion liters every year), there is a strong case for the development of efficient catalysts for the direct oxidation of the bioethanol to acetic acid.^[1,3–17]

Palladium-, copper-, and gold-based catalysts are active in the oxidation of bioethanol.^[3–15] In this oxidation reaction, catalyst stability is the biggest challenge, since the metal nanoparticles easily aggregate into bigger nanoparticles.^[4,5] To overcome this problem, metal catalysts encapsulated in zeolites (M@zeolite) have been designed and prepared.^[18–23] Particularly, S-1 zeolite encapsulating gold nanoparticles was found to be active, stable, and selective for the production of acetaldehyde.^[5] Normally, zeolites encapsulating metal nanoparticles are synthesized under hydrothermal conditions; a process in which utilization of the metal is relatively low (about 34%) and in which polluted water is produced. Recently, a solvent-free strategy for synthesizing various zeolites was reported.^[24–27] Because the solvent (water) is absent in this strategy the production of polluted water is avoided, and hence this strategy is regarded as a green process.^[28]

Herein, we demonstrate the solvent-free synthesis of an S-1 zeolite encapsulating gold–palladium bimetallic nanoparticles (AuPd@S-1), combining the advantages of both M@zeolite catalysts (stability) and a greener synthesis strategy (solvent-free). More than 96% of the gold and palladium in the starting gel are transferred into the AuPd@S-1 product; the catalyst also exhibits superior catalytic activity, unique selectivity, and high stability towards the aerobic oxidation of bioethanol in mixtures with water.

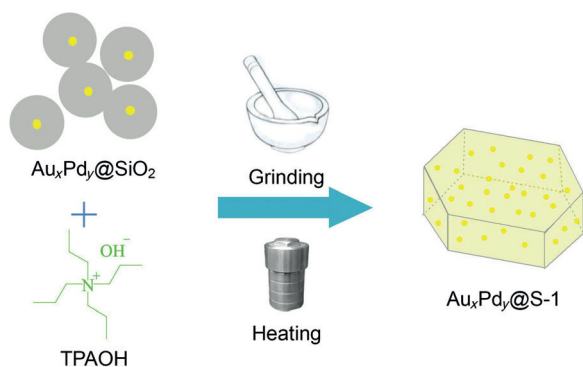
The AuPd@S-1 samples were synthesized by grinding the solid raw materials [bimetallic gold–palladium nanoparticles encapsulated with amorphous SiO₂ (AuPd@SiO₂) and tetrapropylammonium hydroxide (TPAOH)], followed by thermal treatment at 180 °C for 2–4 days (Scheme 1). The gold and palladium contents could be adjusted, and herein we designate our samples as Au_xPd_y@S-1, where *x* and *y* stand for the molar ratio of gold and palladium, respectively.

Figure 1 shows X-ray diffraction (XRD) patterns of the AuPd@S-1 samples. All of the samples exhibit XRD peaks typical for the MFI zeolite structure.^[29,30] It is difficult to observe the peaks related to the Au–Pd nanoparticles, indicating that these Au–Pd nanoparticles are well-dispersed within the S-1 crystals. Table 1 lists the textural parameters and metal loadings of the AuPd@S-1 samples. These samples have high surface areas (349–413 m² g⁻¹) and pore volumes (0.16–0.18 cm³ g⁻¹) (entries 1–6). The total metal loadings in the samples are about 1.5%, and their gold and palladium contents could be effectively adjusted. Through our use of the solvent-free strategy, the utilization of gold and palladium in the samples is above 96%. These results confirm that most of the gold

[a] J. Zhang, Dr. L. Wang, Dr. L. Zhu, Q. Wu, C. Chen, X. Wang, Y. Ji, Dr. X. Meng, Prof. F.-S. Xiao
Key Laboratory of Applied Chemistry of Zhejiang Province
Zhejiang University
Hangzhou 310028 (PR China)
E-mail: liangwang@zju.edu.cn
fsxiao@zju.edu.cn

Supporting Information for this article is available on the WWW under <http://dx.doi.org/10.1002/cssc.201500261>.

This publication is part of a Special Issue on the “Future Energy” conference in Sydney, Australia. To view the complete issue, visit: <http://onlinelibrary.wiley.com/doi/10.1002/cssc.v8.17/issuetoc>.



Scheme 1. Solvent-free synthesis of zeolite crystals encapsulating bimetallic Au–Pd nanoparticles. TPAOH = tetrapropyl ammonium hydroxide.

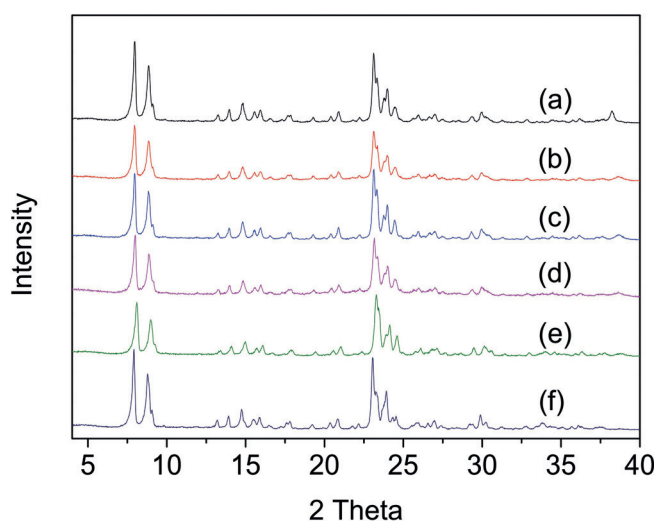


Figure 1. XRD patterns of (a) Au@S-1, (b) Au_{0.6}Pd_{0.4}@S-1, (c) Au_{0.5}Pd_{0.5}@S-1, (d) Au_{0.4}Pd_{0.6}@S-1, (e) Au_{0.2}Pd_{0.8}@S-1, and (f) Pd@S-1.

and palladium species in the raw AuPd@SiO₂ materials are effectively transferred into the AuPd@S-1 product. In contrast, the utilization of gold and palladium reaches only 34–36% in the synthesis of Au_{0.4}Pd_{0.6}@S-1 by a conventional hydrothermal route. This might be due to dissolution of amorphous SiO₂ in the AuPd@SiO₂ under hydrothermal conditions, resulting in leaching of Au–Pd species into the liquor. By contrast, SiO₂ dissolution is negligible under solvent-free conditions, thus giving high metal utilization in the AuPd@S-1 samples.

Entry	Sample	S_{BET} [m ² g ⁻¹]	V_p [cm ³ g ⁻¹]	Metal loading in M@SiO ₂ [wt %] ^[a]		Metal loading in M@S-1 [wt %] ^[a]		Metal utilization [%] ^[b]	
				Au	Pd	Au	Au	Pd	Au
1	Au@S-1	360	0.17	1.50	–	1.50	–	> 99	–
2	Au _{0.6} Pd _{0.4} @S-1	349	0.16	1.10	0.42	1.10	0.41	> 99	97
3	Au _{0.5} Pd _{0.5} @S-1	413	0.17	0.98	0.51	0.96	0.50	98	98
4	Au _{0.4} Pd _{0.6} @S-1	349	0.16	0.81	0.69	0.79	0.66	97	96
5	Au _{0.2} Pd _{0.8} @S-1	362	0.17	0.47	1.01	0.46	1.01	98	> 99
6	Pd@S-1	378	0.18	–	1.50	–	1.50	–	> 99
7	Au _{0.4} Pd _{0.6} /S-1	376	0.18	–	–	0.80	0.70	–	–
8	Au _{0.4} Pd _{0.6} @S-1-HT	376	0.18	2.40	2.01	0.81	0.71	34	36

[a] By ICP analysis. [b] Calculated from metal content in AuPd@S-1/metal content in raw AuPd@SiO₂.

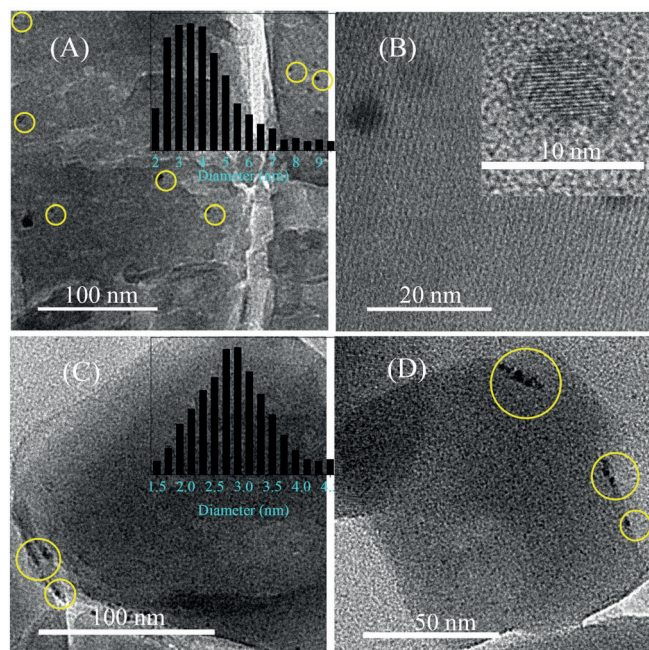


Figure 2. Tomogram section TEM images of (A, B) Au_{0.4}Pd_{0.6}@S-1, and (C, D) Au_{0.4}Pd_{0.6}/S-1. Inserts in (A) and (C): metal particle size distribution. Insert in (B): HRTEM image of Au_{0.4}Pd_{0.6} {111} plane.

Figure 2 shows transmission electron microscopy (TEM) tomography images of the Au_{0.4}Pd_{0.6}@S-1 and Au_{0.4}Pd_{0.6}/S-1 samples. This technique completely avoids the influence of metal nanoparticles on the external surface. In Au_{0.4}Pd_{0.6}@S-1 (Figure 2A, B), Au–Pd nanoparticles can be directly observed, confirming that these particles are indeed encapsulated within the S-1 crystals. STEM images show that the size distribution of the Au–Pd nanoparticles mainly falls in the range 2.5–6.5 nm (Figure 2A, insert and Supporting Information, Figure S1). In Au_{0.4}Pd_{0.6}/S-1, the Au–Pd nanoparticles are found only on the side of the S-1 crystal (Figure 2C, D), indicating that the metal nanoparticles are only located on the external surface of the crystal (Supporting Information, Scheme S1). Similarly, the STEM images show that the Au–Pd nanoparticles in the Au_{0.4}Pd_{0.6}@S-1, Au_{0.5}Pd_{0.5}@S-1, Au_{0.6}Pd_{0.4}@S-1, Au_{0.2}Pd_{0.8}@S-1, and Pd@S-1 samples have a similar metal size distribution (2.5–6.5 nm; Supporting Information, Figure S2–S5). In comparison, monometallic Au nanoparticles on Au@S-1 had a larger size distribution, in the range 3–9 nm (Supporting Information, Figure S6), which agrees well with the fact that addition of palladium to gold nanoparticles significantly reduces the particle size.^[31]

Energy dispersive X-ray (EDX) analysis of the Au_{0.4}Pd_{0.6}@S-1 indicates the presence of both gold and palladium species, and the ratios of gold to palladium are almost unchanged for the randomly selected regions (Sup-

porting Information, Figure S7). Furthermore, the HRTEM image shows that the Au–Pd nanoparticle has a lattice spacing of 0.230 nm for the {111} plane, which falls between the values of 0.239 nm for {111} Au and 0.223 nm for {111} Pd. These results indicate the formation of a bimetallic gold–palladium alloy, rather than separate gold and palladium phases.^[32–34]

Noble-metal nanoparticles usually have a relatively low stability at high temperature (> 500 °C).^[18,19] However, Au_{0.4}Pd_{0.6}@S-1 synthesized by the solvent-free strategy shows extraordinary thermal stability. For example, after calcination at 650 °C for 2 h in air, it is very difficult to observe any change in the size of the nanoparticles in the Au_{0.4}Pd_{0.6}@S-1 samples (Supporting Information, Figure S8). In comparison, Au–Pd nanoparticles on the external surface of S-1 (Au_{0.4}Pd_{0.6}/S-1) became larger after the same treatment (4–20 nm; Supporting Information, Figure S9A). This phenomenon can be attributed to confinement of Au–Pd nanoparticles within the S-1 framework, preventing the aggregation of Au_{0.4}Pd_{0.6}@S-1 at high temperature.

To further understand the structure of Au_{0.4}Pd_{0.6}@S-1, we employed aerobic oxidation of probe molecules of different sizes: benzyl alcohol (BA) and 3,5-dimethyl benzyl alcohol (DMBA). Figure 3A shows catalytic data for the aerobic oxidation of mixed alcohols of BA and DMBA (BA/DMBA at 5) over Au_{0.4}Pd_{0.6}@S-1 and Au_{0.4}Pd_{0.6}/S-1. Notably, both Au_{0.4}Pd_{0.6}@S-1 and Au_{0.4}Pd_{0.6}/S-1 are active for the BA oxidation, giving a conversion higher than 99% at the initial stage of the reaction. However, for the DMBA oxidation, the Au_{0.4}Pd_{0.6}/S-1 is still very active, while the Au_{0.4}Pd_{0.6}@S-1 exhibits very low conversion (ca. 10%). This is because the molecular size of DMBA is larger than the size of the micropores of the S-1 crystals, making it difficult for DMBA molecules to diffuse towards Au–Pd nanoparticles encapsulated within the S-1 crystals (Supporting Information, Figure S13). By contrast, DMBA oxidation is not limited in the case of Au–Pd nanoparticles on the external surface of Au_{0.4}Pd_{0.6}/S-1.^[19,21] Furthermore, after poisoning by 2,4-quinolinediol Au_{0.4}Pd_{0.6}/S-1 nearly loses its activity, while Au_{0.4}Pd_{0.6}@S-1 still exhibits full BA conversion (Figure 3B). These results support the notion that the Au–Pd nanoparticles are encapsulated within the S-1 crystals.

To investigate the stability of the Au_{0.4}Pd_{0.6}@S-1 sample, we investigated the dependence of the activity on reaction time in the BA oxidation, as shown in Figure 4 and Figure S10 (Supporting Information). Au_{0.4}Pd_{0.6}@S-1 and Au_{0.4}Pd_{0.6}/S-1 catalysts are very active, giving full BA conversion (> 99.5%) to benzaldehyde (sole product) at the start of the reaction. After 11 h, the Au_{0.4}Pd_{0.6}@S-1 still exhibits a high BA conversion at 96.0%, with a benzaldehyde selectivity higher than 99.5%. Even after reaction 36 h, Au_{0.4}Pd_{0.6}@S-1 still shows a BA conversion of 76.6% with a benzaldehyde selectivity of 95.0%. After calcination at 500 °C for 2 h in oxygen, the Au_{0.4}Pd_{0.6}@S-1 catalyst completely recovers its catalytic performance through removal of cokes, showing BA conversion and benzaldehyde selectivity values higher than 99.5%. TEM images of Au_{0.4}Pd_{0.6}@S-1 samples after 38 h of reaction show size distributions for the Au–Pd nanoparticle similar to those of as-synthesized samples, indicating the high stability of the nanoparticles encapsulated in

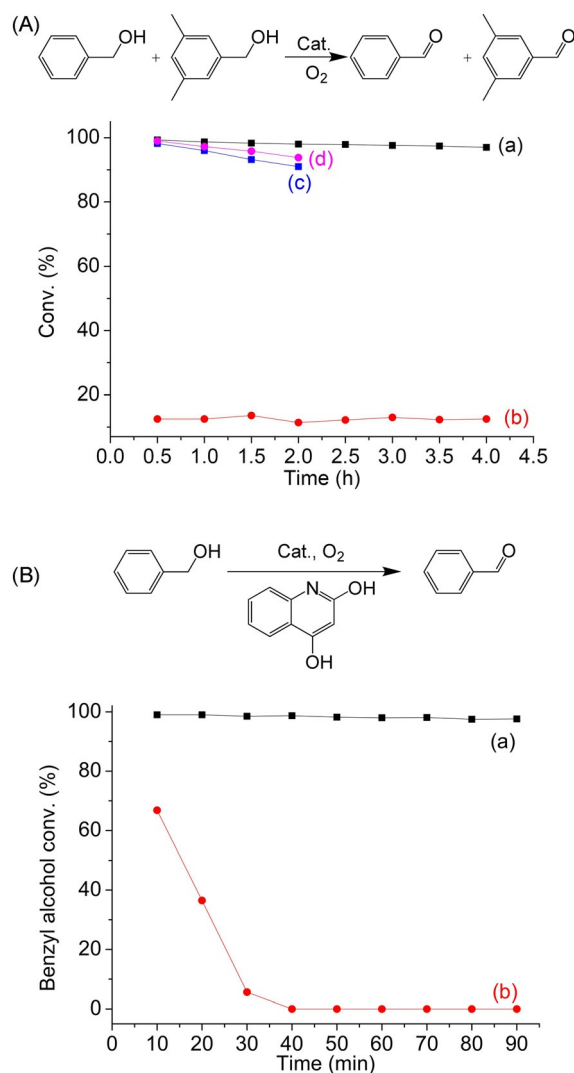


Figure 3. (A) Aerobic oxidation of benzyl alcohol (BA) and 3,5-dimethyl benzyl alcohol (DMBA) over Au_{0.4}Pd_{0.6}@S-1 and Au_{0.4}Pd_{0.6}/S-1 at mixed alcohol inlet rate at 0.12 mL h⁻¹ (BA/DMBA at 5), 0.2 g of catalyst, O₂ flow rate at 5 mL min⁻¹, 220 °C. (a) BA and (b) DMBA conversion over Au_{0.4}Pd_{0.6}@S-1, (c) BA and (d) DMBA conversion over Au_{0.4}Pd_{0.6}/S-1. (B) Aerobic oxidation of BA in the presence of 2,4-quinolinediol over (a) Au_{0.4}Pd_{0.6}@S-1 and (b) Au_{0.4}Pd_{0.6}/S-1 catalysts. The mixture (BA/2,4-quinolinediol at 98) inlet rate at 0.12 mL h⁻¹, 0.2 g of catalyst, O₂ flow rate at 5 mL min⁻¹, 220 °C.

the S-1 crystals (Figure S1B). In contrast, the BA conversion and benzaldehyde selectivity over Au_{0.4}Pd_{0.6}/S-1 decreased with increasing reaction time. After 6 h, Au_{0.4}Pd_{0.6}/S-1 gave a BA conversion and a benzaldehyde selectivity of 71.5 and 82.3%, respectively. Calcination in oxygen did not recover the catalytic performance of Au_{0.4}Pd_{0.6}/S-1. Because metal leaching was not detected during the reaction (Supporting Information, Table S1), the deactivation of Au_{0.4}Pd_{0.6}/S-1 should be related to aggregation of the Au–Pd nanoparticles during the reaction, as evidenced by a sample TEM image (Figure S9B).

Figure 5A shows the dependence of catalytic activity on reaction temperature in the oxidation of bioethanol over Au_{0.4}Pd_{0.6}@S-1. When the temperature is lower than 170 °C, the catalyst is nearly inactive. When the reaction temperature

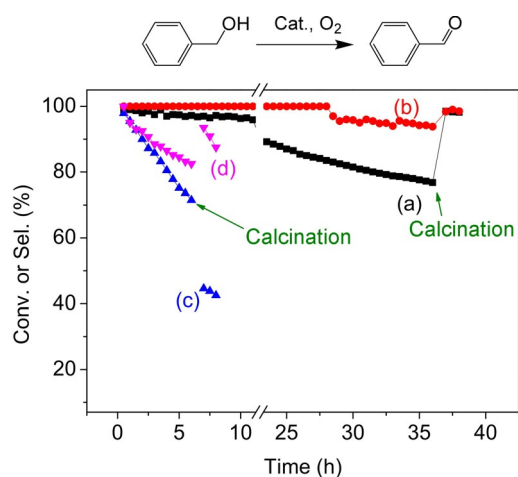


Figure 4. Dependence of BA conversion and benzaldehyde selectivity on reaction time in aerobic oxidation of BA over $\text{Au}_{0.4}\text{Pd}_{0.6}/\text{S-1}$ and $\text{Au}_{0.4}\text{Pd}_{0.6}/\text{S-1}$ catalysts. BA inlet rate of 0.12 mL h^{-1} , 0.2 g of catalyst, O_2 flow rate of 5 mL min^{-1} , 220°C . (a) BA conversion and (b) benzaldehyde selectivity over $\text{Au}_{0.4}\text{Pd}_{0.6}/\text{S-1}$, (c) BA conversion and (d) benzaldehyde selectivity over $\text{Au}_{0.4}\text{Pd}_{0.6}/\text{S-1}$.

reaches 200°C , the ethanol conversion is 92.8%, which is much higher than the value reported for a gold nanoparticle catalyst (ca. 50%) at the same reaction temperature.^[5] This can be attributed to the higher activity of bimetallic Au–Pd nanoparticles compared to monometallic Au nanoparticles in alcohol oxidations.^[31–34] Interestingly, $\text{Au}_{0.4}\text{Pd}_{0.6}/\text{S-1}$ gave a very high selectivity for the formation of acetic acid. At 200°C , the selectivity for acetic acid was 96.7%; when the temperature was higher than 210°C , the selectivity was higher than 99.0%, which is even higher than that over $\text{Au}/\text{MgAl}_2\text{O}_4$, one of the most efficient catalyst for the oxidation of ethanol to acetic acid (Supporting Information, Table S2).^[6] This process offers a route for the selective oxidation of bioethanol to acetic acid with ideal atomic economy. Figure 5B shows the dependence of conversion and selectivity on reaction time in the oxidation of bioethanol over $\text{Au}_{0.4}\text{Pd}_{0.6}/\text{S-1}$. The catalyst retains its activity and selectivity even after 50 h, indicating its extraordinarily high stability (Supporting Information, Figure S11).

Crude bioethanol produced by fermentation is well-known to contain water, and separating ethanol from water is an energy-consuming process.^[35] Therefore, it is preferred that the ethanol oxidation reaction is performed using crude bioethanol (i.e., a mixture of ethanol and water) as feedstock. Figure 6 shows the dependence of product yields on reaction time in the oxidation of bioethanol (a mixture of water and ethanol as model substrate) containing various water contents over $\text{Au}_{0.4}\text{Pd}_{0.6}/\text{S-1}$ and $\text{Au}_{0.4}\text{Pd}_{0.6}/\text{S-1}$. In the case of $\text{Au}_{0.4}\text{Pd}_{0.6}/\text{S-1}$, there is little influence for the catalytic conversion of the bioethanol. When 20% water is present in the feedstock, $\text{Au}_{0.4}\text{Pd}_{0.6}/\text{S-1}$ gives an ethanol conversion of 85% and a selectivity to acetic acid of 94%. When the water content reaches 90%, $\text{Au}_{0.4}\text{Pd}_{0.6}/\text{S-1}$ still exhibits an ethanol conversion of 82% and an acetic acid selectivity of 94%. This is due to the hydrophobicity of the S-1 zeolite, which enables to efficiently separate the ethanol and water,^[36,37] hindering access of water to

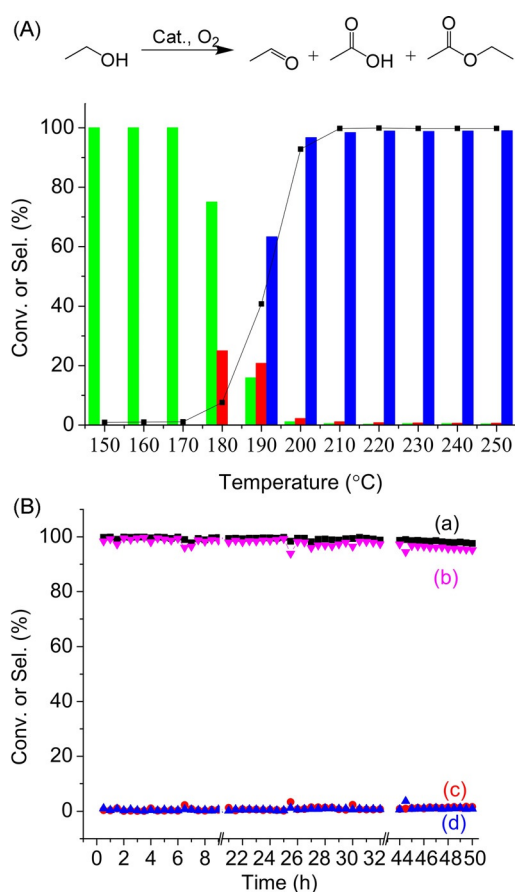


Figure 5. (A) Dependences of ethanol conversion (black line) and selectivities for acetic acid (blue column), ethyl acetate (red column), and acetaldehyde (green column). (B) Dependences of (a) catalytic conversion and selectivities for (b) acetic acid, (c) ethyl acetate, and (d) acetaldehyde on the time in the bioethanol oxidation over $\text{Au}_{0.4}\text{Pd}_{0.6}/\text{S-1}$ at ethanol inlet rate of 0.12 mL h^{-1} , 80 mg of $\text{Au}_{0.4}\text{Pd}_{0.6}/\text{S-1}$, O_2 rate of 8 mL min^{-1} , 215°C .

the Au–Pd nanoparticles in the zeolite’s micropores. In comparison, the $\text{Au}_{0.4}\text{Pd}_{0.6}/\text{S-1}$ catalyst is strongly influenced by the presence of water in the bioethanol. When 20% water was added to the feedstock, the $\text{Au}_{0.4}\text{Pd}_{0.6}/\text{S-1}$ catalyst showed an ethanol conversion of 17% and an acetic acid selectivity of 32%; when 90% water was added, ethanol conversion was as low as 2%. The excellent water tolerance of $\text{Au}_{0.4}\text{Pd}_{0.6}/\text{S-1}$ is important for catalytic applications involving crude bioethanols in the future.

Figure 6 shows how after reaction for 30 h in the presence of water, when pure ethanol is introduced as feedstock, $\text{Au}_{0.4}\text{Pd}_{0.6}/\text{S-1}$ still exhibits a very high conversion (97.5%) and selectivity (95.8%) to acetic acid, while $\text{Au}_{0.4}\text{Pd}_{0.6}/\text{S-1}$ shows a much lower conversion (40.0%) and selectivity (68%). The poor recovery of catalytic performance over $\text{Au}_{0.4}\text{Pd}_{0.6}/\text{S-1}$ catalyst is assigned to the aggregation of the Au–Pd nanoparticles in the presence of water.

In conclusion, a solvent-free strategy is successfully used to synthesize S-1 zeolite crystals encapsulating bimetallic gold–palladium nanoparticles ($\text{Au}_{0.4}\text{Pd}_{0.6}/\text{S-1}$). Compared to the conventional hydrothermal route, the solvent-free strategy allows efficient use of the noble metals and significantly reduces the

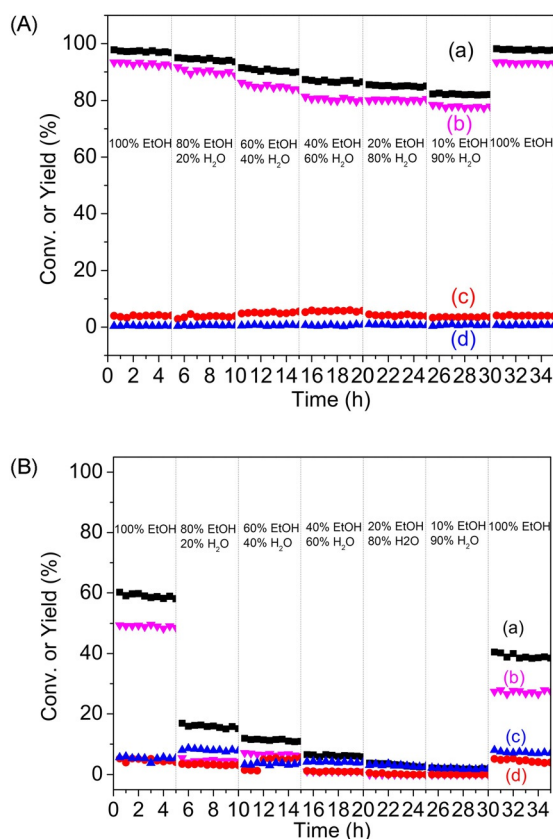


Figure 6. Dependences of (a) ethanol conversion and selectivities for (b) acetic acid, (c) ethyl acetate, and (d) acetaldehyde on the time in the bioethanol oxidation over (A) $\text{Au}_{0.4}\text{Pd}_{0.6}@S-1$ and (B) $\text{Au}_{0.4}\text{Pd}_{0.6}/S-1$. Ethanol inlet rate at 0.12 mL h^{-1} , 60 mg of catalyst, O_2 rate at 8 mL min^{-1} , 220°C .

volume of polluted water produced in the synthesis. More importantly, in the aerobic oxidation of bioethanol the $\text{Au}_{0.4}\text{Pd}_{0.6}@S-1$ catalyst exhibits excellent activity, a very high selectivity for acetic acid, and extraordinary stability. Particularly, the $\text{Au}_{0.4}\text{Pd}_{0.6}@S-1$ catalyst has superior tolerance for water, as demonstrated by bioethanol conversions in the presence of large amounts of water. These features are important for future practical applications of these zeolite crystals encapsulating metals as catalysts.

Acknowledgements

This work is supported by National Natural Science Foundation of China (21403192 and U146220026), National High-Tech Research and Development program of China (2013AA065301).

Keywords: biomass conversion · gold · nanoparticles · palladium · zeolites

- [1] A. Corma, S. Iborra, A. Velty, *Chem. Rev.* **2007**, *107*, 2411–2502.
- [2] J.-P. Tessonnier, A. Villa, O. Najoulet, D. S. Su, R. Schlögl, *Angew. Chem. Int. Ed.* **2009**, *48*, 6543–6546; *Angew. Chem.* **2009**, *121*, 6665–6668.
- [3] J. Zhang, X. Liu, M. Sun, X. Ma, Y. Han, *ACS Catal.* **2012**, *2*, 1698–1702.
- [4] P. Liu, E. J. M. Hensen, *J. Am. Chem. Soc.* **2013**, *135*, 14032–14035.

- [5] J. Mielby, J. O. Abildström, F. Wang, T. Kasama, C. Weidenthaler, S. Kegnæs, *Angew. Chem. Int. Ed.* **2014**, *53*, 12513–12516; *Angew. Chem.* **2014**, *126*, 12721–12724.
- [6] B. Jørgensen, S. E. Christiansen, M. L. Thomsen, C. H. Christensen, *J. Catal.* **2007**, *251*, 332–337.
- [7] O. A. Simakova, V. I. Sobolev, K. Y. Koltunov, B. Campo, A.-R. Leino, K. Kordás, D. Y. Murzin, *ChemCatChem* **2010**, *2*, 1535–1538.
- [8] C. H. Christensen, B. Jørgensen, J. Rass-Hansen, K. Egeblad, R. Madsen, S. K. Klitgaard, S. M. Hansen, M. R. Hansen, H. C. Andersen, A. Riisager, *Angew. Chem. Int. Ed.* **2006**, *45*, 4648–4651; *Angew. Chem.* **2006**, *118*, 4764–4767.
- [9] V. I. Sobolev, K. Y. Koltunov, O. A. Simakova, A.-R. Leino, D. Y. Murzin, *Appl. Catal. A* **2012**, *433–434*, 88–95.
- [10] N. Zheng, G. D. Stucky, *J. Am. Chem. Soc.* **2006**, *128*, 14278–14280.
- [11] J. Gong, C. B. Mullins, *J. Am. Chem. Soc.* **2008**, *130*, 16458–16459.
- [12] X. M. Kong, L. L. Shen, *Catal. Commun.* **2012**, *24*, 34–37.
- [13] T. Takei, N. Iguchi, M. Haruta, *New J. Chem.* **2011**, *35*, 2227–2233.
- [14] X. H. He, H. C. Liu, *Catal. Today* **2014**, *233*, 133–139.
- [15] J. C. Bauer, G. M. Veith, L. F. Allard, Y. Oyola, S. H. Overbury, S. Dai, *ACS Catal.* **2012**, *2*, 2537–2546.
- [16] J. Rass-Hansen, H. Falsig, B. Jørgensen, C. H. Christensen, *J. Chem. Technol. Biotechnol.* **2007**, *82*, 329–333.
- [17] J. Sun, K. Zhu, F. Gao, C. Wang, J. Liu, C. H. F. Peden, Y. Wang, *J. Am. Chem. Soc.* **2011**, *133*, 11096–11099.
- [18] A. B. Laursen, K. T. Højholt, L. F. Lundegaard, S. B. Simonsen, S. Helveg, F. Schüth, M. Paul, G.-D. Grunwald, S. Kegnæs, C. H. Christensen, K. Egeblad, *Angew. Chem. Int. Ed.* **2010**, *49*, 3504–3507; *Angew. Chem.* **2010**, *122*, 3582–3585.
- [19] S. Li, L. Burel, C. Aquino, A. Tuel, F. Morfin, J.-L. Rouselet, D. Farrusseng, *Chem. Commun.* **2013**, *49*, 8507–8509.
- [20] S. Li, T. Boucheron, A. Tuel, D. Farrusseng, F. Meunier, *Chem. Commun.* **2014**, *50*, 1824–1826.
- [21] J. Shi, X. Li, Q. R. Wang, Y. H. Zhang, Y. Tang, *J. Catal.* **2012**, *291*, 87–94.
- [22] P. Sun, G. Gao, Z. Zhao, C. Xia, F. Li, *ACS Catal.* **2014**, *4*, 4136–4142.
- [23] Z. Wu, S. Goel, M. Choi, E. Iglesia, *J. Catal.* **2014**, *311*, 458–468.
- [24] L. Ren, Q. Wu, C. Yang, L. Zhu, C. Li, P. Zhang, H. Zhang, X. Meng, F.-S. Xiao, *J. Am. Chem. Soc.* **2012**, *134*, 15173–15176.
- [25] Y. Jin, Q. Sun, G. Qi, C. Yang, J. Xu, F. Chen, X. Meng, F. Deng, F.-S. Xiao, *Angew. Chem. Int. Ed.* **2013**, *52*, 9172–9175; *Angew. Chem.* **2013**, *125*, 9342–9345.
- [26] Q. Wu, X. Wang, G. Qi, Q. Guo, S. Pan, X. Meng, J. Xu, F. Deng, F. Fan, Z. Feng, C. Li, S. Maurer, U. Müller, F.-S. Xiao, *J. Am. Chem. Soc.* **2014**, *136*, 4019–4025.
- [27] Y. Jin, X. Chen, Q. Sun, N. Sheng, Y. Liu, C. Bian, F. Chen, X. Meng, F.-S. Xiao, *Chem. Eur. J.* **2014**, *20*, 17616–17623.
- [28] X. Meng, F.-S. Xiao, *Chem. Rev.* **2014**, *114*, 1521–1543.
- [29] P. Y. Dapsens, C. Mondelli, J. Pérez-Ramírez, *ChemSusChem* **2013**, *6*, 831–839.
- [30] E. Kim, J. Choi, M. Tsapatsis, *Microporous Mesoporous Mater.* **2013**, *170*, 1–8.
- [31] Y. Feng, H. Yin, D. Gao, A. Wang, L. Shen, M. Meng, *J. Catal.* **2014**, *316*, 67–77.
- [32] L. Shi, A. Wang, T. Zhang, B. Zhang, D. S. Su, H. Li, Y. Song, *J. Phys. Chem. C* **2013**, *117*, 12526–12536.
- [33] L. Wang, W. Zhang, S. Zeng, D. S. Su, X. Meng, F. S. Xiao, *Chin. J. Chem.* **2012**, *30*, 2189–2197.
- [34] J. Huang, Y. Zhu, M. Lin, Q. Wang, L. Zhao, Y. Yang, K. X. Yao, Y. Han, *J. Am. Chem. Soc.* **2013**, *135*, 8552–8561.
- [35] S. Kumar, N. Singh, R. Prasad, *Renewable Sustainable Energy Rev.* **2010**, *14*, 1830–1844.
- [36] J. Kuhn, S. Sutanto, J. Gascon, J. Gross, F. Kapteijn, *J. Membr. Sci.* **2009**, *339*, 261–274.
- [37] B. Soydaş, Ö. Dede, A. Çulfaz, H. Kalıpçılar, *Microporous Mesoporous Mater.* **2010**, *127*, 96–103.

Received: February 17, 2015

Published online on June 3, 2015